

Title	The influence of carrier density and doping type on lithium insertion and extraction processes at silicon surfaces
Authors	McSweeney, William;Lotty, Olan;Glynn, Colm;Geaney, Hugh;Holmes, Justin D.;O'Dwyer, Colm
Publication date	2014-05-17
Original Citation	McSweeney, W., Lotty, O., Glynn, C., Geaney, H., Holmes, J. D. and O'Dwyer, C. (2014) 'The influence of carrier density and doping type on lithium insertion and extraction processes at silicon surfaces', <i>Electrochimica Acta</i> , 135, pp. 356-367. doi: 10.1016/j.electacta.2014.05.035
Type of publication	Article (peer-reviewed)
Link to publisher's version	http://www.sciencedirect.com/science/article/pii/S0013468614010196 - 10.1016/j.electacta.2014.05.035
Rights	© 2014 Elsevier Ltd. All rights reserved. This manuscript version is made available under the CC-BY-NC-ND 4.0 license. - http://creativecommons.org/licenses/by-nc-nd/4.0/
Download date	2024-04-10 23:06:42
Item downloaded from	https://hdl.handle.net/10468/6115

The influence of carrier density and doping type on lithium insertion and extraction processes at silicon surfaces

W. McSweeney^{1,2,3}, O. Lotty^{1,4}, C. Glynn^{1,4}, H. Geaney^{1,4}, J. D. Holmes^{1,4,5}, and C. O'Dwyer^{1,3,4*}

¹ *Department of Chemistry, University College Cork, Cork, Ireland*

² *Department of Physics and Energy, University of Limerick, Limerick, Ireland*

³ *Materials and Surface Science Institute, University of Limerick, Limerick, Ireland*

⁴ *Micro & Nanoelectronics Centre, Tyndall National Institute, Lee Maltings, Cork, Ireland*

⁵ *Centre for Research on Adaptive Nanostructures and Nanodevices (CRANN), Trinity College Dublin, Dublin 2, Ireland*

*** Corresponding author:** Colm O'Dwyer, Department of Chemistry, and Tyndall National Institute, University College Cork, Cork, Ireland. Tel: +353 (0)21 4902732; Fax: +353 (0)21 4274097; email: c.odwyer@ucc.ie

Abstract

The Li^+ insertion and extraction characteristics at n-type and p-type Si(100) electrodes with different carrier density and doping type are investigated by cyclic voltammetry and constant current measurements. The insertion and extraction potentials are demonstrated to vary with cycling and the occurrence of an activation effect in the n-type electrodes where the charge capacity and voltammetric currents are found to be much higher than p-type electrodes. A rate-dependent redox process influenced by the surface region electronic density, which influences the magnitude of cyclic voltammetry current is found at Si(100) surface regions during Li insertion and extraction. At p-type Si(100) surface regions, a thin, uniform film forms at lower currents, while also showing a consistently high (>70%) Coulombic efficiency for Li extraction. The p-type Si(100) surface region does not undergo crack formation after deintercalation and the amorphization was demonstrated using transmission electron microscopy (TEM). X-ray photoelectron spectroscopy (XPS) and Raman scattering demonstrate that highly doped n-type Si(100) retains Li as a silicide and converts to an amorphous phase as a two-step phase conversion process. The findings show the succinct dependence of Li insertion and extraction processes for uniformly doped Si(100) single crystals and how the doping type and its effect on the semiconductor-solution interface dominate Li insertion and extraction, composition, crystallinity changes and charge capacity.

I. Introduction

Rechargeable Li-ion batteries are prevailing as the power source of choice for portable electronics and hybrid electrical vehicles[1-7]. For mobile applications, high energy (per weight and volume) is the most important parameter since it determines the usage time per charge[8]. Compared to other technologies, Li-ion batteries (LIBs) have a high energy density, good cycle life, and good power performance[1-3, 9-11]. The LIB performance involves interrelated electrochemistry, phase transitions and transport processes at the interfaces between electrodes and electrolytes[12].

To improve the performance of LIBs, improved understanding of the behaviour of active materials is sought. Bulk lithium (Li) alloy type anodes comprising of elemental Sn, Ge, Si or their alloys showed their functionality as LIB anodes with large specific and volumetric capacities[13].

Silicon (Si) is an attractive anode material for LIBs because it has a relatively low potential range at which charge occurs, below 0.5 V[14] when reacting with Li. Si is known to incorporate a theoretical maximum of 4.4 Li atoms per Si atom [14], resulting in the highest known theoretical charge capacity ($4,200 \text{ mAh g}^{-1}$)[15] which is more than ten times higher than the capacity of graphite (372 mAh g^{-1}) and much higher than alternative oxide materials[16, 17]. In addition to its high capacity, Si is the second most abundant element in the earth's crust, is environmentally benign and there is already a mature industrial infrastructure in existence, which also makes it an attractive material when considering commercial applications. $\text{Li}_{15}\text{Si}_4$ is the highest lithiated phase achievable for the ambient temperature lithiation of bulk Si and corresponds to a capacity of 3579 mAh g^{-1} [18]. When bulk Si is fully lithiated to $\text{Li}_{15}\text{Si}_4$ it undergoes a volume expansion of $\sim 280\text{--}300\%$ and has a maximum theoretical volumetric capacity of 2190 mAh cm^{-3} . Unfortunately, Si electrodes pulverize due to this large expansion and contraction upon Li insertion and extraction and this

causes the electrode material to lose contact with the current collector, resulting in a decrease in charge storage capacity over time[13, 19-26].

Several Si structures have been investigated as a viable anode for LIBs, including Si nanopillars[27], Si powder[28, 29], Si wafers that were ball milled into Si powder[30], Si thin films[31, 32], Si nanowires (NWs)[33-35], core-shell Si NWs[36, 37], Si nanotubes[38], Si nanoparticles[39] and Si NWs decorated with Si nanoparticles[40]. Recent investigations have involved the use of hollow structures and so-called clamped structures (the structures have a SiO_x coating layer which prevents the Si from expanding outward while still allowing Li ions to pass through) in an effort to improve cyclability, solid electrolyte interface (SEI) layer formation and its influence on phase transformation[41]. Materials with defined porosity could also potentially compensate for large swing changes in morphology of the active material[42]. Si NWs grown on current collectors[21, 43] by vapour-liquid-solid (VLS) growth have shown some promise in circumventing these issues as they inherently reduce the Li insertion distances, and to some extent can expand and contract thus reducing the degree pulverization; 1D Si materials however, exhibit a strongly anisotropic expansion along the [110] direction during lithiation [44, 45].

While the VLS method is straightforward and reasonably controlled, the Si NWs produced are generally intrinsically doped and therefore not very conductive. Controlled doping methodologies, which can be difficult to implement for several NW growth methods on the scale required by commercial batteries, or the use of conductive additives, are required to improve conductivity and electrical addressing in the active materials[46] for the entirety of the active material, even under compression in an assembled cell. Additionally, there is limited information in the literature concerning Si crystal orientation, carrier concentration and dopant type on the Li insertion and extraction processes.

Doping type and density modify these insertion and extraction processes, and in nanoscale systems all of the abovementioned parameters, including doping control, can vary from nanostructure to nanostructure[47]. Etching of bulk wafers is one method to improve doping control, orientation and electrical contact. Peng et al.[46] and Flake et al.[48, 49] reported Si NW anodes fabricated by metal assisted chemical (MAC) etching of Si wafers. This method has the potential for precise control of crystal orientation and doping [46, 50, 51]. Density functional theory and related modelling have confirmed a crystal orientation influence on Li insertion in a variety of materials[52], leading to prediction of cell potentials, favoured higher rate insertion facets, and links between the Li uptake and the crystallographic phase change. Amorphization, morphology changes and secondary electrolyte interphases can occur during reversible lithiation. A first principles study suggests that dopants can have an effect on the binding energy of Li with Si[53]. A systematic examination of doping on many aspects of Li insertion and extraction in Si is still required.

An important characteristic of Si is its doping density, which is directly related via its carrier mobility, to its conductivity. The conductivity of Si anodes is typically varied by introducing a conductive additive (often a carbon)[39, 54-56], which are often required for intrinsically doped or low conductivity materials and structures [57]. Doping NWs to increase their electrical conductivity has also been shown to improve capacity retention at high charge/discharge rates[34]. Few studies exist on the lithiation of doped Si in nanostructured form as dispersed powder mixtures, often involving amorphous Si[58] or polycrystalline nano Si-graphite mixtures[59, 60] and related nanoscale Si analogues. The doping contribution to conductivity and Li uptake (reduction of Li upon insertion at the cost of an electron) is difficult to separate from enhanced electrical conductivity of the entire material matrix, which becomes continually hole-doped while changing its structure, composition and electrical nature. This is further complicated by changes in active material contacts within the matrix,

the random, uneven distribution of conductive additives in powder materials, and the inconsistency in rational doping of some forms of Si.

In this work, we report a systematic investigation of Li insertion and extraction at Si(100) single-crystal surface regions. The findings detail the comparative difference in the structural and electrochemical response to lithiation in both lightly doped p-type and heavily doped n-type electrodes. Cyclic voltammetry analysis at various potential sweep rates also shows how differently doped Si(100) surface regions influence the redox processes of Li insertion and extraction and we also show using electron microscopy how the response of the Si(100) surface region to phase changes and crystalline-to-amorphous deformation from lithium silicide formation is doping dependent. Voltammetry avoids strong polarization by comparison to (high) constant current tests where the applied current is greater than the magnitude of the voltammetric current at low scan rates that approximate a steady state system. We also present detailed spectroscopic analysis of crystal structure and surface region composition post-cycling and detail the succinct influence of doping type and doping density on the galvanostatic response of Si(100) surface region to electrochemical lithiation when used as a battery anode.

II. Experimental

200 mm p-type B-doped Si(100) wafers (680 μm thickness) with a resistivity of 5 – 80 $\Omega\text{ cm}$, corresponding to a doping density between $1.6 - 70 \times 10^{14}\text{ cm}^{-3}$, and n-type As-doped Si(100) wafers with a resistivity of 0.001 – 0.005 $\Omega\text{ cm}$, corresponding to a doping density of between $1.2 - 7.4 \times 10^{19}\text{ cm}^{-3}$ were cleaved into 1 cm^2 electrodes. The backside SiO_2 was removed using a diamond scribe and Indium-Gallium (In-Ga) eutectic paste was applied to the back of the Si electrode to form a low resistance electrical contact.

Electrochemical experiments were carried out using a split cell contained in an Argon atmosphere. Li foil was used as the counter electrode in a half-cell configuration. Unless otherwise stated, all measurements are referenced to Li^+/Li electrode. A porous separator soaked in an electrolyte comprising of $1 \text{ mol dm}^{-3} \text{ LiPF}_6$ in a mixture of ethylene carbonate–diethyl carbonate (EC:DEC 1:1 v/v) was used. Measurements were recorded using a CHI 660B potentiostat and a BioLogic VSP. P-type and n-type Si(100) wafer electrodes underwent cyclic voltammetry (CV) at varying scan rates between 0.5 mV s^{-1} and 10 mV s^{-1} between 2 V and 0 V for 30 cycles. In all cases the data (unless stated otherwise) is shown between 1.5 V and 0 V. Galvanostatic measurements were also carried out on p-type and n-type Si electrodes to determine their voltage profiles, their capacity values and capacity retention over numerous cycles. The Si(100)-electrolyte flat-band potential and effective carrier concentrations in the cell were determined using electrochemical capacitance-voltage measurements in the framework of the Mott-Schottky model ($1/C^2$ vs. V) by applying a potential equivalent to the flatband potential of the interface (i.e. depletion conditions). The potentials were applied at a rate of 10 mV s^{-1} with a superimposed a.c. signal with an amplitude of 15 mV.

Scanning electron microscopy (SEM) of lithiated Si samples was conducted with a Hitachi S4800 FESEM operating at 5 kV. Cross-sectioning of the Si electrodes post electrochemical cycling was carried out with an FEI Helios Nanolab Dual Beam FIB System. A protective layer of platinum was deposited over the surface of the sample to minimize surface damage. Cross-sectional TEM sample preparation was performed on the slice using a standard FIB lift out technique described elsewhere[61]. TEM was conducted at 200 kV using a JEOL TEM JEM-2100.

Raman scattering spectroscopy of pristine and cycled Si(100) n- and p-type electrodes was conducted using a Dilor XY Labram spectrometer equipped with an Olympus BX40

confocal microscope and Renishaw InVia Raman spectrometer using a RenCam CCD camera. Excitation was provided by 514 nm ArHe 10 mW green laser with a maximum of 0.512 mW incident power. The spectra are collected with a Peltier cooled CCD detector. The incident power of the laser was adjusted using calibrated filters.

XPS was conducted using a VG Escalab 220i-XL instrument equipped with a dual anode (Mg/Al) source. Charge compensated photoelectron spectra were acquired for O 2s and Li 1s core-levels. Peaks were fitted with Voigt profiles using a Shirley background correction.

III. Results and Discussion

A. Cyclic voltammetry and cycling of p-type and n-type Si(100)

Figure 1 shows the characteristic CVs of p-type and n-type Si (100) in the LiPF₆-containing electrolyte for their first cycle. When the electrode was cycled from 2.0 – 0.0 V vs. Li⁺/Li, a significant increase in cathodic current was observed due to the formation of Li-Si phases. The anodic peaks are due to the deformation of these phases as the Li is being extracted. The cathodic current related to Li insertion for p-type Si increases at ~0.3 V indicating that it is forming the Li_{2.33}Si phase[62], while the single anodic peak at ~0.5 V corresponds to the deformation of this Li_{2.33}Si phase[63]. For the n-type Si, cathodic current does not increase until ~0.1 V, but it increases dramatically, forming a high Li mole fraction Li-Si phase in a narrow insertion potential window. Characteristically, for n-type Si(100), the high mole fraction Li_{3.25}Si phase forms and two anodic peaks on the reverse scan at ~0.3 V and 0.5 V corresponding to delithiation of this phase[21].

To determine the effective carrier concentration at the interface between the Si(100) and 1 mol dm⁻³ LiPF₆ in 50:50 EC:DMC, capacitance-voltage analysis was performed under

depletion conditions. Doping densities at the interface were extracted from the slope of Figures 1(c) and (d) according to $N_{D,A} = 2/m q \epsilon_s \epsilon_0$, which is interpreted from the Mott Schottky equation[64], where $N_{D,A}$ is the doping density of either n- or p-type Si, m is the slope of $1/C^2$ vs. V , q is the electronic charge, ϵ_s is the dielectric constant for Si and ϵ_0 is the permittivity of free space.

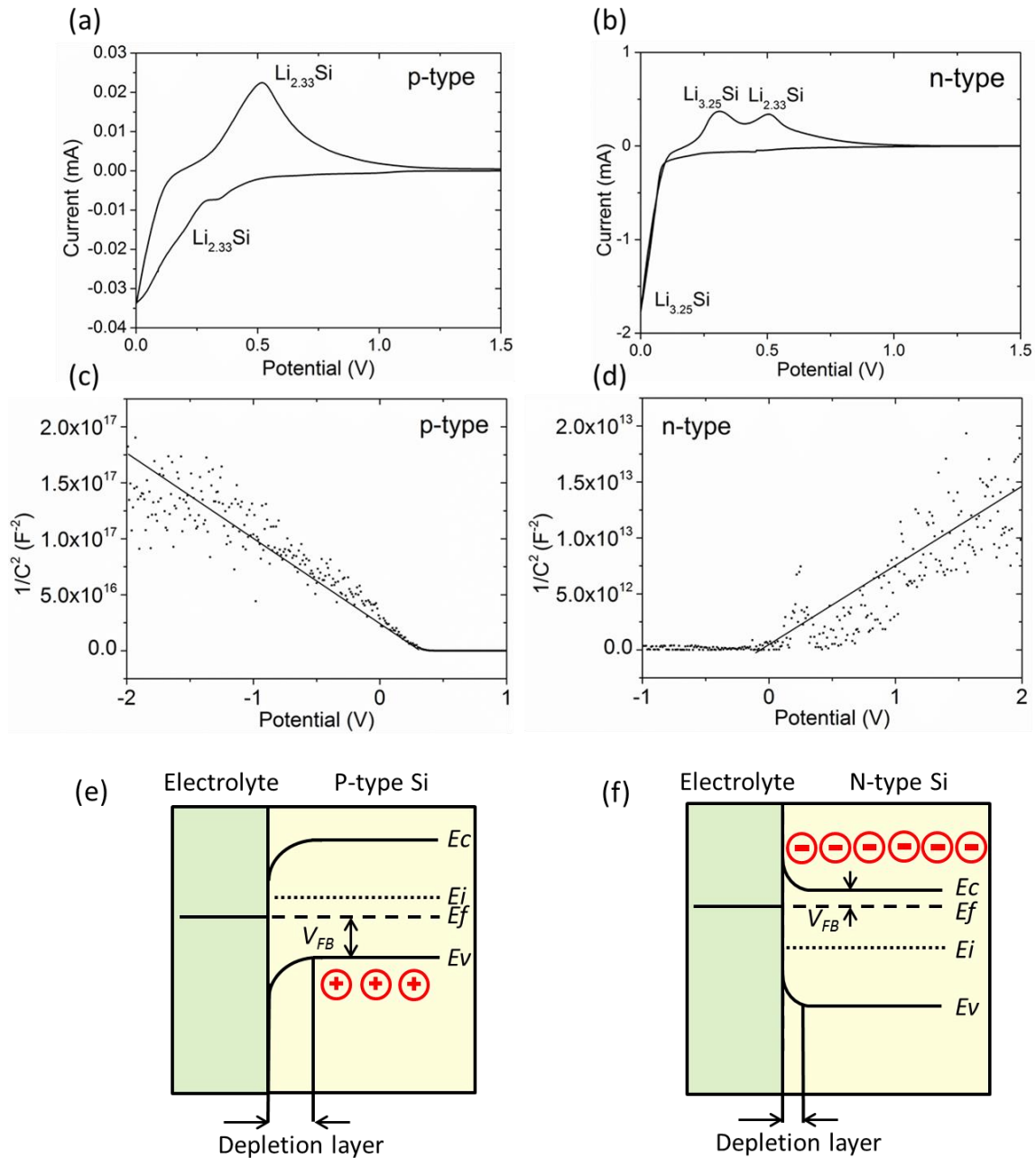


Figure 1. Cyclic voltammograms of (a) p-type Si and (b) n-type Si acquired in the potential range 2 – 0 V at a scan rate of 1 mV s^{-1} . Characteristic Li-Si phases associated with cathodic and anodic peaks are indicated. Figs. c and d show the Mott-Schottky plots of the p-type and

n-type Si(100) electrodes, respectively, indicating the difference in dopant type, doping densities, and flat-band potential V_{fb} . Figs. e and f are schematics of the band diagrams of p-type and n-type Si-electrolyte interfaces respectively, showing the effect of dopant and doping density on the energy levels of Si. E_c is conduction band energy, E_f is the Fermi level, E_v is the valence band, E_i is the intrinsic Fermi level and V_{FB} is the flatband potential.

Measurements of the flat band potential, V_{fb} (the potential difference between the Fermi energy and that of the Si surface at the electrolyte) are extracted from the abscissa intercept. From the slopes of graphs obtained from Figs. (c) and (d), we calculated the effective doping density at the electrolyte interface of the p-type Si to be approximately $1 \times 10^{14} \text{ cm}^{-3}$ and that of the n-type Si to be $4 \times 10^{18} \text{ cm}^{-3}$. The flat band potential was calculated to be 0.27 V for the p-type Si(100) and -0.07 V for the n-type Si(100) in the electrolyte. A narrow depletion region (shown for n- and p-type si in Figs e and f) and lower barrier (in-built potential) relative to the redox potential E_{redox}^0 , and n-type Si(100) is expected to offer an improved rate of Li^+ reduction at the surface region (a higher electronic density available for Li^+ at the surface). The difference in V_{fb} between n- and p-type Si(100) in this electrolyte is found to be much less than the bandgap energy of Si. Schematics of the band diagrams at the Si-electrolyte interface are shown in Figs. (e) and (f). These schematics also illustrate the difference in the depletion layer width (narrower for n-type) and the work function between the highly doped n-type Si and low doped p-type Si with reference to the electrolyte.

The different lithiation voltages in Figs. 1(a) and (b) are due to the relative positions of the Fermi levels in the n-type and p-type Si and that of the redox potential for Li^+/Li in solution. The difference in band-bending at the interface (Figs 1e,f) affects the lithiation voltages. Considering the more negative flat-band potential of the n-type Si(100) to that of the Li^+/Li redox potential ($\sim 0.1 \text{ V}$ and 0.3 V for p-type and n-type respectively) and the higher energy of the n-type Fermi level, the energy barrier to electron transfer (rate of Li^+ uptake) at the interface to reduce a Li ion is lower for n-type electrodes. The current response

in Fig. 1(b) is also higher than the current response in 1(a) due to the higher doping density of the n-type Si ($N_D = 1.2 \times 10^{19} \text{ cm}^{-3} - 7.4 \times 10^{19} \text{ cm}^{-3}$) compared to the doping density of the p-type Si ($N_A = 1.6 \times 10^{14} \text{ cm}^{-3} - 7.0 \times 10^{15} \text{ cm}^{-3}$). The effective surface carrier density directly affects the rate uptake of Li^+ implying that more Li^+ can be intercalated/alloyed per unit time for more conductive Si. This is balanced between the available electron density at the Si surface, the potential difference and any energetic barrier for charge transfer, the solid state diffusion limit for Li in Si, and by any concentration polarization effects caused by a large, crowded Li^+ concentration at the surface prior to uptake by the Si. Surface orientation ((100) versus (111) for instance) is known to have negligible effect on the chemical potential for Li insertion into Si [63].

As the potential was varied at low scan rates and thus relatively low currents, we assume that the electrode potential predominantly represents the Li activity at the surface region, and that internal resistance drops across the electrode are constant and negligible by comparison.

Figure 2(a-c) shows the p-type Si cycled at varying scan rates for 30 cycles each. The p-type Si retains the general voltammetric shape shown in Fig. 1(a) throughout cycling and this is also maintained at higher scan rates. Each consecutive cycle results in the current of both the anodic and cathodic peaks to increase in magnitude. As will be detailed below in Section C, p-type Si(100) does not undergo significant cracking. Since the density of Li reaction at the surface region is related to the doping density, which for the p-type Si is quite low, the rate of Li insertion is not maximized in the first cycle and thus allows continual lithiation in each cycle even without large scale cracking of the p-type Si(100). Investigations by McDowell et al. of a single Si NW battery, have suggested that the lithiation rate decreases with time and its origins are believed to be due to a lithiation process that is an interfacial reaction, which ordinarily sets a limit to the lithiation rate [65, 66]. In effect, when

pulverization causes stress fields, this rate can decrease during extended lithiation times. Our work identifies a doping influence on such processes, specifically at a defined (100) Si surface region of much larger surface area than a single NW.

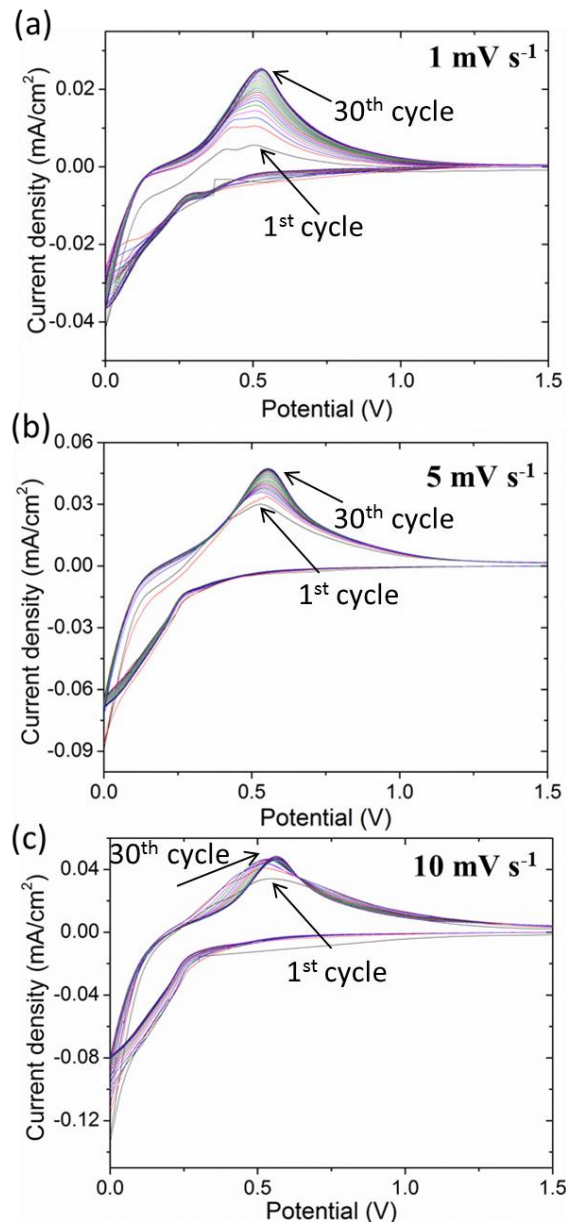


Figure 2. Cyclic voltammetry of p-type Si(100) electrodes cycled from 2 V to 0 V for 30 cycles at (a) 1 mV s^{-1} (b) 5 mV s^{-1} and (c) 10 mV s^{-1} .

The current (reaction rate) associated with Li insertion and extraction becomes greater with increasing potential scan rate. This observation confirms that the initial lithiation and delithitation reaction rates (current density) are dependent on the scan rate of the applied

potential. Successive cycling shows a reduction in the difference between the magnitude of the 1st and 30th cycle current values (delithiation to $\text{Li}_{2.33}\text{Si}$) at successively higher scan rates.

A stable and continuous SEI layer is considered as a crucial factor in the performance of an LIB as it provides a protective passivation layer that prevents further electrolyte decomposition and allows ion conduction for Li^+ insertion and extraction as well as maintaining anode integrity[67, 68]. On Si, like many anode materials, SEI formation predominantly takes place during the first ‘charge’ cycle, corresponding to the first cathodic sweep of the CV in this study. As SEI formation occurs at higher potentials to Li insertion, and crack development results in (re)formation of SEI prior to Li insertion. The responses at scan rates at 1 mV s^{-1} and 5 mV s^{-1} are significantly slower than the 10 mV s^{-1} scan rate and therefore the formation of the SEI layer is less evident in Figs. 2(a,b). These data indicate that the SEI film formation of the Si surface region is rate dependent. In Fig. 2(c) the cathodic current density between 1.0 V and $\sim 0.3 \text{ V}$ on the first cycle is higher than subsequent cycles at the higher scan rate which is possibly due to the formation of the SEI layer.

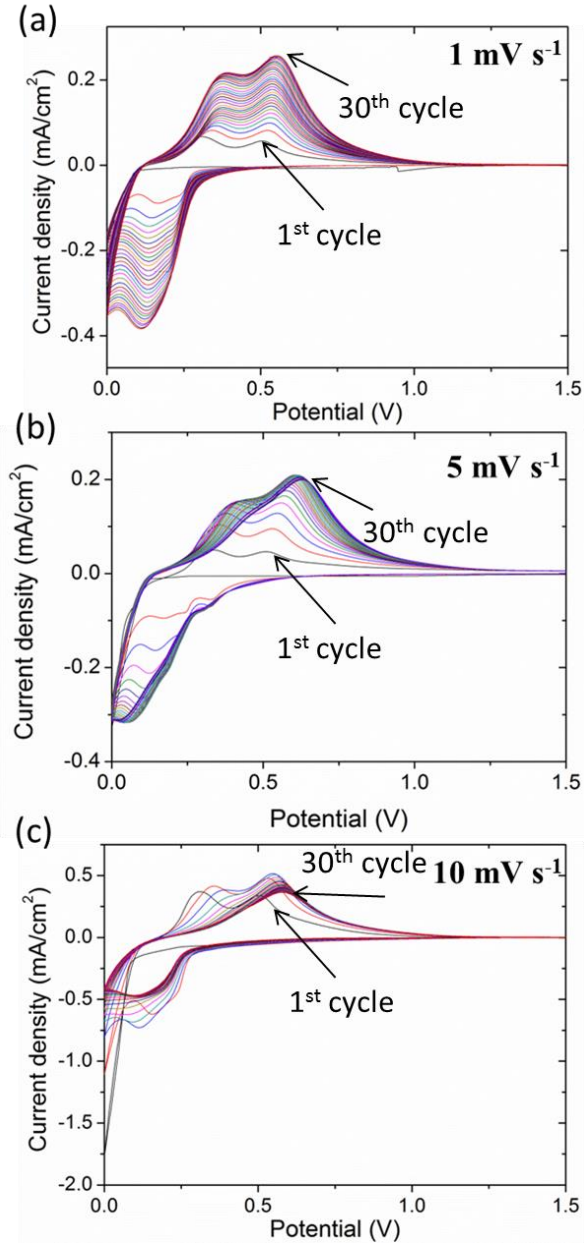


Figure 3. Cyclic voltammetry of n-type Si electrodes cycled from 2 V to 0 V for 30 cycles at (a) 1 mV s⁻¹ (b) 5 mV s⁻¹ and (c) 10 mV s⁻¹.

Figure 3(a-c) shows the n-type Si cycled at a series of scan rates for 30 cycles each. The 1st cycle retains the overall voltammetric response shown in Fig. 1(b) for n-type Si(100). After the 2nd cycle, the peak at 0.14 V, which is characteristically absent at the first cycle, indicates the crystal-to-amorphous transition[18, 69] as Si converts to a lithium silicide. The cathodic current reaches a maximum at ~0.14 V indicating full insertion to form the Li_{2.33}Si

phase, and subsequently decreases. The cathodic current begins to increase again at ~ 0.05 V and we believe this to be the formation of a second Li-Si phase $\text{Li}_{3.25}\text{Si}$. On the anodic scan two delithiation peaks are observed at ~ 0.37 V and ~ 0.5 V corresponding to change in phase from $\text{Li}_{3.25}\text{Si}$ and $\text{Li}_{2.33}\text{Si}$ respectively. It is noticeable the current values for the n-type Si electrodes are much larger than p-type electrodes at any scan rate. This effect is primarily due to the difference in doping densities, and therefore conductivities of the two electrodes and their rate capability for Li uptake, which is greater for n-type Si. Similar to the p-type Si(100), the n-type Si(100) currents increase with cycling, and the magnitude of the currents is found to increase also with higher scan rates for each comparative cycle number. Additionally, we consistently find that in p-type and n-type Si(100) electrodes, the degree of current increase per cycle reduces as the scan rate is increased, and the effect is more clearly observed in higher doped n-type electrodes (Fig. 3(c)). These characteristics are related to the activation of the Si, where Li ions can access more Si with each CV scan and therefore the current response increases with cycling.

By measuring the peak cathodic values of the 2nd cycle and the 30th cycle we can demonstrate how this activation process varies with scan rate and doping density. We calculate that for the p-type Si(100) electrode scanned at 1 mV s^{-1} scan, the cathodic peak current for insertion increases by 0.014 mA, for the 5 mV s^{-1} scan, the current increased by 0.013 mA, and for the 10 mV s^{-1} scan, the current increased by 7.36 μA . Whereas for the n-type, we calculated that for the 1 mV s^{-1} scan, the cathodic peak current increases by 0.172 mA, for the 5 mV s^{-1} scan, the current increased by 0.097 mA and for the 10 mV s^{-1} scan, the current actually decreased by 0.112 mA. This demonstrates that the “activation” process is greater at slower scan rates and is also greater for Si with a higher doping density.

In Fig. 3(c) we observe a dramatic shift in the voltages for both Li insertion and extraction and a decrease in the peak current with cycling. At higher scan rates, the definition

of both Li insertion and extraction peaks is reduced and a single peak is observed for each overall process. The average voltage at which the cathodic peak current occurs for the p-type Si is 0.518 V at 1 mV s⁻¹, 0.548 V at 5 mV s⁻¹ and 0.554 V at 10 mV s⁻¹. For the n-type Si, the corresponding peak voltages are 0.538 V at 1 mV s⁻¹, 0.560 V at 5 mV s⁻¹ and 0.571 V at 10 mV s⁻¹, i.e. consistently higher at faster scan rates in both electrodes between scan rate of 1 – 10 mV s⁻¹. This average positive shift in insertion voltage for increased scan rates from 1 mV s⁻¹ to 10 mV s⁻¹ is approximately the same for the p-type ($\Delta V_p = 36$ mV) and n-type ($\Delta V_n = 33$ mV) Si. We believe this increase in voltage is due to the polarization of the anode.

The p-type and n-type Si(100) electrodes used in this study are B-doped and As-doped, respectively and computational density functional theory studies [63] on the effect of dopant segregation at the Si(100) surface show that for B and P-doped Si(100), Li insertion deeper into p-type Si is more favourable due to having a lower chemical potential. For n-type Si(100) a higher Li insertion rate per unit time is possible with the formation of Zintl Li-Si phases occurring in parallel. Such investigations also concluded that Li insertion into p-type Si(100) should occur at slightly higher potentials, but from Figs. 1-3, we find that the exact Li insertion potential is difficult to define due to its convoluted nature. Certainly, in p-type electrodes, the onset of Li insertion occurs at a higher potential than in the n-type electrodes, which agrees with the influence of a higher n-type doping with a correspondingly lower potential barrier and thus lower overvoltage required for the Li⁺/Li redox process observed in CVs. Higher mole fraction Li-Si phases are possible for n-type electrodes and the doping density type and concentration, under slowly varying potentially driven interaction, self-limits the relative capacity of lithiation in single crystal Si(100). These effects might also vary in nanoscale silicons where crystal orientation and doping profiles can be controlled.

B. Li redox insertion and extraction rates in n- and p-type Si(100)

Both n-type and p-type Si electrodes were cycled at various scan rates between 0.5 mV s⁻¹ and 10 mV s⁻¹ in order to relate the reversibility of the redox process involving Li⁺/Li and its relationship to effective solution and solid-state diffusion on the Li insertion and extraction processes. The cathodic and anodic peak currents are related to the diffusion coefficients for Li⁺/Li redox process (insertion and extraction via reduction and oxidation) from n-type and p-type Si(100) according to the Randles-Ševčík relations[70-72]:

$$i_p = (2.69 \times 10^5) n(n_\alpha \alpha)^{3/2} A D^{1/2} C v^{1/2} \text{ and } \frac{dV_p}{d \ln v} \propto 0.03/\alpha$$

where i_p is the peak current in amps, n is number of electrons transferred in the redox event, A is the electrode area in cm², D is the diffusion coefficient in cm² s⁻¹, C is the concentration in mol dm³, α is the transfer coefficient, typically = 0.5 and v is the scan rate in V s⁻¹.

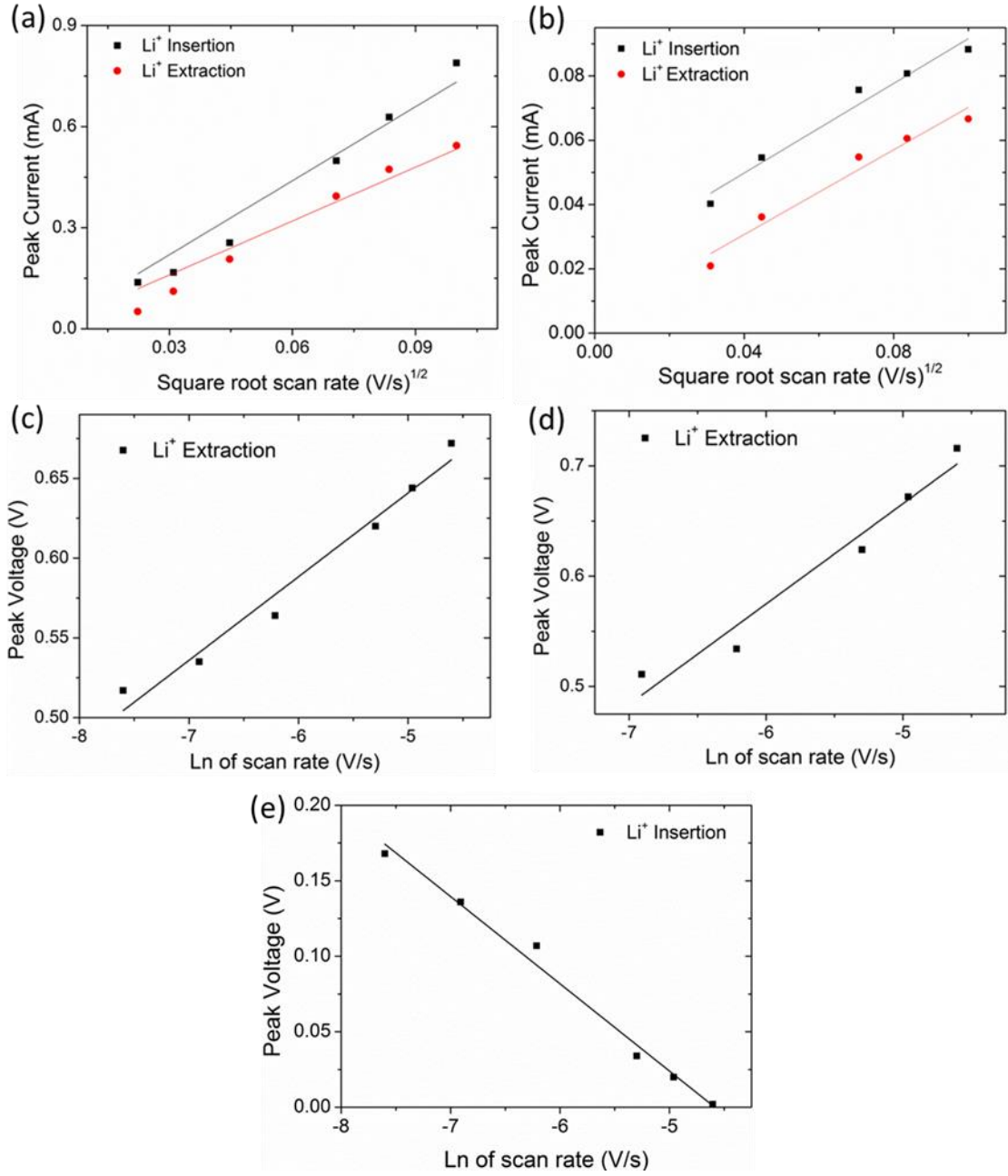


Figure 4. Peak current, I_p as a function of the scan rate ($v^{1/2}$) for Li insertion and extraction at (a) n-type and (b) p-type Si(100) surface regions. The variation of the corresponding peak potential V_p with $\ln v$ is also shown in (c) for the p-type Si and (d) for the n-type Si, respectively. (e) The variation of the insertion peak potential for the n-type Si with $\ln v$.

Figure 4 shows the variation of I_p with $v^{1/2}$ for both Li⁺ insertion and extraction for n-type and p-type Si(100) electrodes cycled successively at increasing scan rates and the variation of V_p with the natural log of the scan rate. In Fig. 4a, the calculated Li⁺ coefficients are $\sim 10.6 \times 10^{-13} \text{ cm}^2 \text{ s}^{-1}$ and $\sim 5.6 \times 10^{-13} \text{ cm}^2 \text{ s}^{-1}$ for insertion and extraction ($\text{Li}^0 \rightarrow \text{Li}^+ + \text{e}^-$)

at n-type Si(100), respectively. We note that in the case of Li extraction, it is the Li^0 extracted (contribution of an electron to the measured current) from delithiating phases on the electrode material that is considered by this analysis. During delithiation, the redox process analysed using this approach corresponds to ionic diffusion since reduced Li in Li-Si phases deeper within the surface film are required to diffuse to the electrolyte interface to contribute to the current. The diffusion value for Li^+ insertion into p-type Si is estimated to be $\sim 6 \times 10^{-11} \text{ cm}^2 \text{ s}^{-1}$ and a value of $\sim 3 \times 10^{-11} \text{ cm}^2 \text{ s}^{-1}$ is found for its extraction (Fig. 4b). The corresponding potential peak shifts associated with the Faradaic-type currents are also shown for both electrode systems in Figs. 4(c) and (d). The trend exhibits some non-linearity most probably due to the slight change in the surface region of the Si in each cycle as the scan rate is increased. Overall, the voltage variation follows the voltage shift seen in CVs (33-36 mV) which is expected from a diffusion-controlled process. For both the n-type and p-type electrodes, the ratio of diffusion-limited cation insertion to extraction is ~ 2 . The higher diffusion rates for the n-type Si are related to the higher electronic concentration compared to the p-type Si, in spite of the lithiated phase on p-Si(100) being much thinner. As was observed from cyclic voltammetry in Figs. 1-3, and examined microstructurally in Section C, the two order-of-magnitude difference in Li diffusion coefficient is related to the ability of the more conductive, higher electron density n-type Si(100) to intercalate Li into high mole fraction Li-Si phases. The Li-diffusion coefficients calculated in the present work are comparable with those estimated for Li^+ diffusion in deposited Si thin films (10^{-13} to $10^{-10} \text{ cm}^2 \text{ s}^{-1}$ [73, 74]) and other materials[75, 76]. As shown in Figs. 2 and 3, the diffusional limitation associated with Li insertion and extraction is also found when the process is driven at very high rates. No peaks associated with these processes are found at the higher scan rates. Figure 4(e) demonstrates a linear relationship between the Li insertion potential for n-type Si(100) consistent with a diffusion process for the n-type Si(100) surface region, where

the insertion potential is lowered at higher scan rates. A Li insertion potential for the p-type Si was not attainable because the insertion potential is convoluted and occurs very near 0 V.

C. Morphology change of n- and p-type Si(100) surface region during lithiation

Figure 5 shows SEM images of the Si surface morphology after CV cycling. After the first cycle both the n- and p-type Si surfaces appear roughened as shown in Fig. 5(a) and (c), possibly due to the formation of the SEI layer (*cf.* Fig. 1). However, in Fig. 5(b) there is clear cracking of the n-type Si(100) surface after 30 cycles, whereas the p-type Si(100) surface shown in Fig. 5(d) retains its integrity after 30 cycles apart from some surface roughening. As more Li^+ is inserted in to the n-type Si when compared to the p-type Si, a greater expansion and contraction of the n-type Si(100) during cycling occurs causing the cracking of the anode[22-24]. The observation of a volume expansion in n-type Si(100) suggests an anisotropic volume or phase change mechanism, which for amorphous Li-Si phases is known to be anisotropic [77], but it is not found in p-type Si(100) even though it is an identical crystal. Isotropic expansion typically follows an amorphous-to-crystalline Li-Si phase conversion [78, 79] and is limited (for an identical (100) orientation at least) to p-type Si in this work. An atomic force microscopy (AFM) study of the anode surface has revealed that cracking occurs during the Li-extraction stage [80-82]. Results presented here under CV conditions show that this cracking is unique to the heavily doped n-type Si(100), and remarkably, the p-type Si(100) surface region remains relatively unaffected. From analysis of SEM images, we calculate that ~37% of the surface area of n-Si(100) in Fig. 5(b) is composed of cracks/voids.

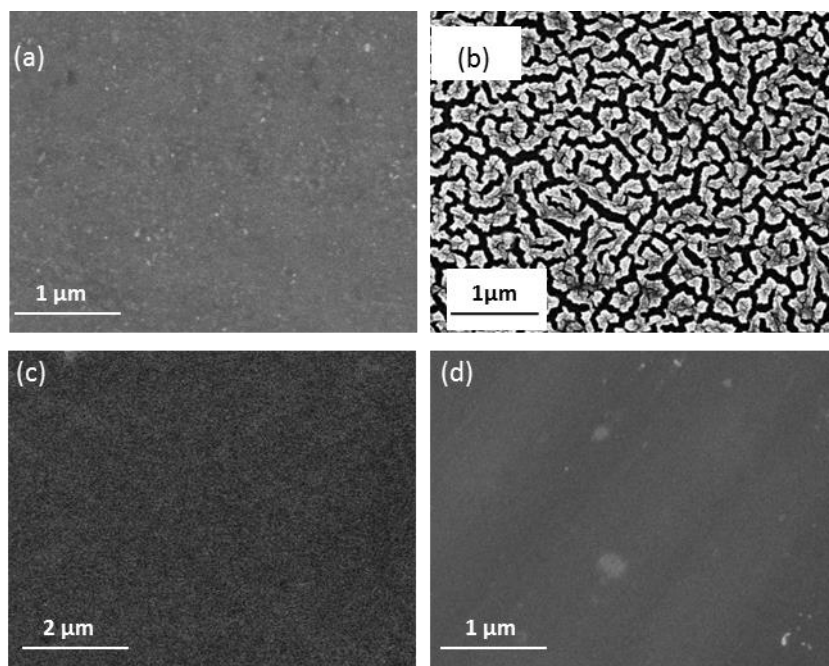


Figure 5. SEM images of n-type Si after (a) 1 cycle, (b) 30 cycles and of p-type Si after (c) 1 cycle, (d) 30 cycles. The scan rate used in each instance was 1 mV s^{-1} .

Intrinsic Si has shown relatively low capacities, as shown in a Si thin film where its reversible capacity fell to $\sim 1850 \text{ mAh g}^{-1}$ after 5 cycles[32] this suggests that doping density could play an important role in the capacity of Si anodes. Since intrinsic Si is a poor electrical conductor, Szczech et al. proposed that it is more favourable to further lithiate regions containing the Li-Si alloys before initially lithiating fresh Si, this could lead to large stresses resulting from expansion of the anode and cause a cracking of the anode and a loss of capacity. Doped Si should encourage more uniform lithiation of the electrode, and therefore provide a more reversible cycling of the anodes [25]. In addition, at very high charge/discharge rates, lower conductivity of Si would compromise electrode performance and result in reduced capacity. Our findings suggest that a trade-off exists between obtaining a crack free surface using lowly doped p-type Si, but at the expense of reduced specific capacities compared to heavily doped n-type Si which can undergo significant structural and crystalline-to-amorphous phase changes and cracking.

Amorphous Si thin films have homogenous volume changes during cycling[19], thereby giving excellent capacity retention as reported in the literature[83, 84]. However, it may not be practical to make amorphous Si in bulk for commercial uses, and knowledge of the doping, insertion facet and their effects on the stability of the material during cycling are important considerations. Limthongkul et al. reported crystalline Si was found to become amorphous upon the first reaction with Li[85, 86], a unique feature that makes crystalline Si a promising negative electrode material. In NWs, the radially changing interfacial reaction remains amorphous until the $\text{Li}_{3.75}\text{Si}$ composition is reached.

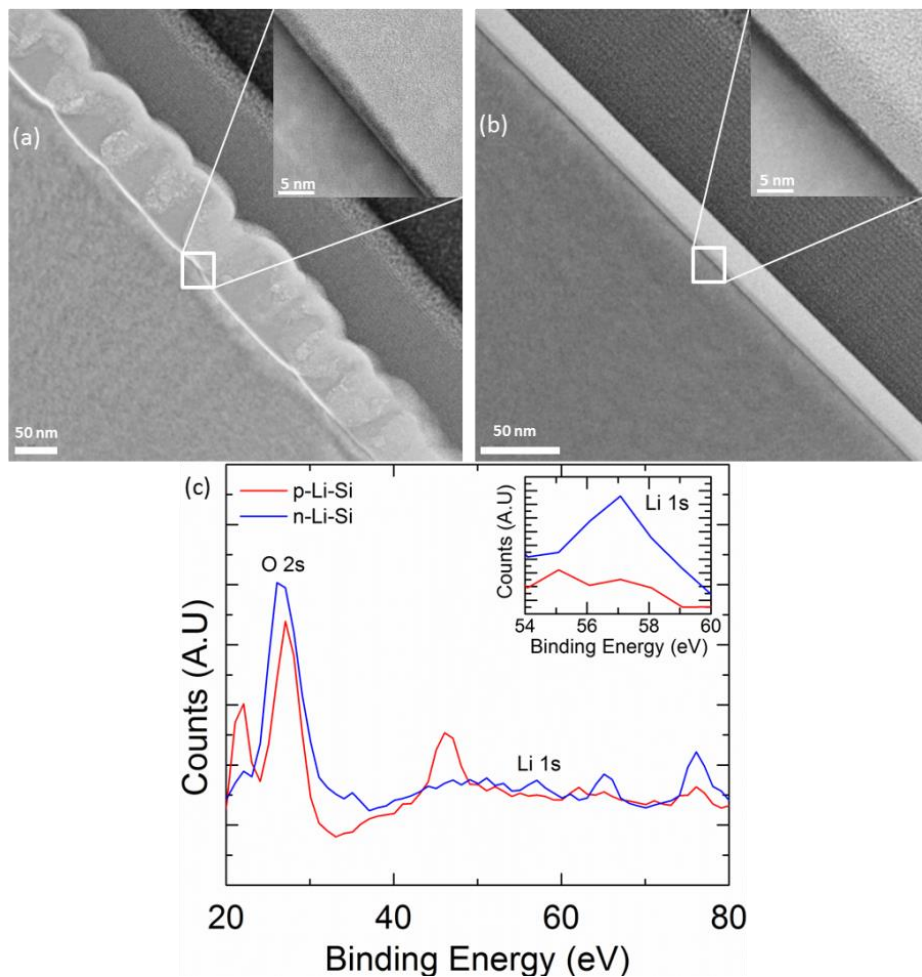


Figure 6. TEM images of (a) n-type Si and (b) p-type Si after 30 cycles showing the depth of Li^+ insertion into the Si(100) surface region with the insets showing the interface between the cycled and uncycled Si, and (c) XPS response from varying regions in cycled n-type and p-type Si (100).

Both p-type and n-type Si(100) electrodes that were cycled for 30 scans at 1 mV s^{-1} were examined using TEM to compare the difference in surface region morphology as a function of dopant type under identical conditions. The white regions in Figs. 6(a) and (b) represent areas of the samples that underwent lithiation during the CV process. In the n-type Si electrode (Fig. 6(a)) the white region appears rough which is in agreement with our SEM imaging of the cracked, pillared surface region. The white region is 80–110 nm in thickness corresponding to the depth of the reacted Li-Si phase. Whereas with the p-type Si electrode (Fig. 6(b)) the white region appears relatively smooth, uncracked, and has an approximate thickness of 28 nm.

Although complicated by one of the phases being amorphous, the interface appears to be atomically abrupt, with a step change from the Li-Si phase to the Si substrate; no obvious phase segregation is evident. This is further corroborated by detailed XPS measurements, which confirm a highly efficient Li extraction from the Li-Si phase on the p-Si(100) electrode surface region as shown in Fig. 6(c). The Li 1s core-level emission peak at $\sim 57 \text{ eV}$ is observed in the cycled n-type Si but not in the p-type Si. The TEM data corroborates the reduced current values from p-type electrodes, and thus a thinner Li-Si phase is found. However, XPS measurements show that an efficient deintercalation process occurs from p-Si.

The Li silicide phases, whether polycrystalline or amorphous, are typically Zintl phase compounds (ZPC), which are intermetallic compounds of metalloids such as Si. The amorphous ZPC film is deformable by comparison to its polycrystalline counterpart and has been found to be less susceptible to stress-induced cracking when the unit cell volume drastically changes during high mole fraction Li insertion into Si. The diffusion coefficient, D , for Li in crystalline Si is $\sim 10^{-14} \text{ cm}^2 \text{ s}^{-1}$, and the diffusional mobility of Li in an already formed ZPC is expected to be faster. Previous investigations by Green et al.[27] have estimated that a possible Li diffusion value of $\sim 10^{-12} \text{ cm}^2 \text{ s}^{-1}$ would be expected in lithium

silicide. Our examination of the Li diffusion constants in Section B above, show that a faster Li redox process is possible in the silicide phases formed on the heavily doped n-type Si(100). Although the electron density and lower potential barrier allow a higher Li intercalation rate and the formation of a thicker layer, the cracking that forms during each deintercalation activates, or opens up, fresh Si for the subsequent charge step. The diffusion length of Li^0 , $L = \sqrt{D\tau}$, where D is the diffusion constant estimated for each electrode. Using the values of D for n- and p-type Si(100), and approximating, we estimate τ as the time taken for the reduction of the Li^+ to occur at the same scan rate, i.e. ~ 200 s at 1 mV s^{-1} *cf.* Fig. 3a. This gives a value of ~ 6 nm for the Li diffusion length in n-type Si(100), but it is ~ 2 orders of magnitude smaller in p-type Si(100). These values also give an estimate for the very small thickness of the Li-Si phase formed in the first cathodic sweep of the electrodes, assuming full Faradaic efficiency of the process.

D. Raman scattering of lithiation in n- and p-type Si(100)

Raman scattering spectroscopy was carried out on cycled and on pristine Si(100) samples to probe the crystal-to-amorphous phase transitions during lithiation. Amorphization of Si anodes typically occurs during the first charge. Previous work has shown that the volume expansion is anisotropic if the phase transition is crystalline-to-amorphous, but isotropic if the initial Si material is already amorphous [41]. Phonon scattering is significantly reduced in amorphous Si, specifically at a particular frequency such as the TO phonon.[63, 87] Raman scattering was previously used to demonstrate the transition from crystalline to amorphous Si in a carbon composite by monitoring the TO c-Si phonon mode [87]. Recently it was shown using Raman scattering that Li inserts anisotropically into single crystalline Si[88]. Figures 7(a,b) show the Raman spectra of pristine p-type Si, of p-type Si after 1 CV cycle and after 30 CV cycles at 1 mV s^{-1} . The TO phonon mode exhibits reduced relative intensity by $\sim 18\%$

indicating a reduction in phonon scattering from along the same wave vector by amorphization in the Si crystal.

Site specific investigations of the lithiation of Si(100) were also conducted. Figures 7(c,d) show the Raman spectra of the pristine n-type Si, n-type Si after 1 CV cycle and two regions (region 1 and 2 as shown in Fig. 7(e)) after 30 CV cycles at 1 mV s^{-1} . In agreement with earlier microscopy analysis, there is a much greater decrease in n-type TO mode (65%) when compared to the p-type Si after 30 cycles. The cycled n-type Si exhibits peaks at $\sim 470 \text{ cm}^{-1}$ and $\sim 150 \text{ cm}^{-1}$ corresponding to altered phonon scattering within amorphous Si[89, 90]. No shift is found in the TO mode ascribed to various phonon scattering mechanisms or size effects, and no stress-induced shifting is observed. Figures 7f(i-iii) show the mapping of the two regions (1+2) shown in Fig. 7(e). Figure 7f(i) shows the intensities of the regions mapped at 200 cm^{-1} (amorphous Si peak) showing the higher intensities in region 2 opposed to region 1 suggesting that region 2 is amorphous compared to the crystalline region in region 1. Figure 7f(ii) is similar to that of 7f(i), except the data is acquired at 470 cm^{-1} (amorphous Si peak). Figure 7f(iii) confirms the intensities at 520 cm^{-1} (crystalline Si) showing that region 1 has a higher crystalline peak than region 2. The Raman scattering evidence identifies that the Li-Si phase formed at the highly doped n-type Si(100) surface region after cycling eventually becomes amorphous. Since a crystalline (100) surface-to-amorphous transition should be accompanied by anisotropic volumetric expansion, a thin continuous layer without cracking shows no indications of crack formation that is typically an indicator of stress relief.

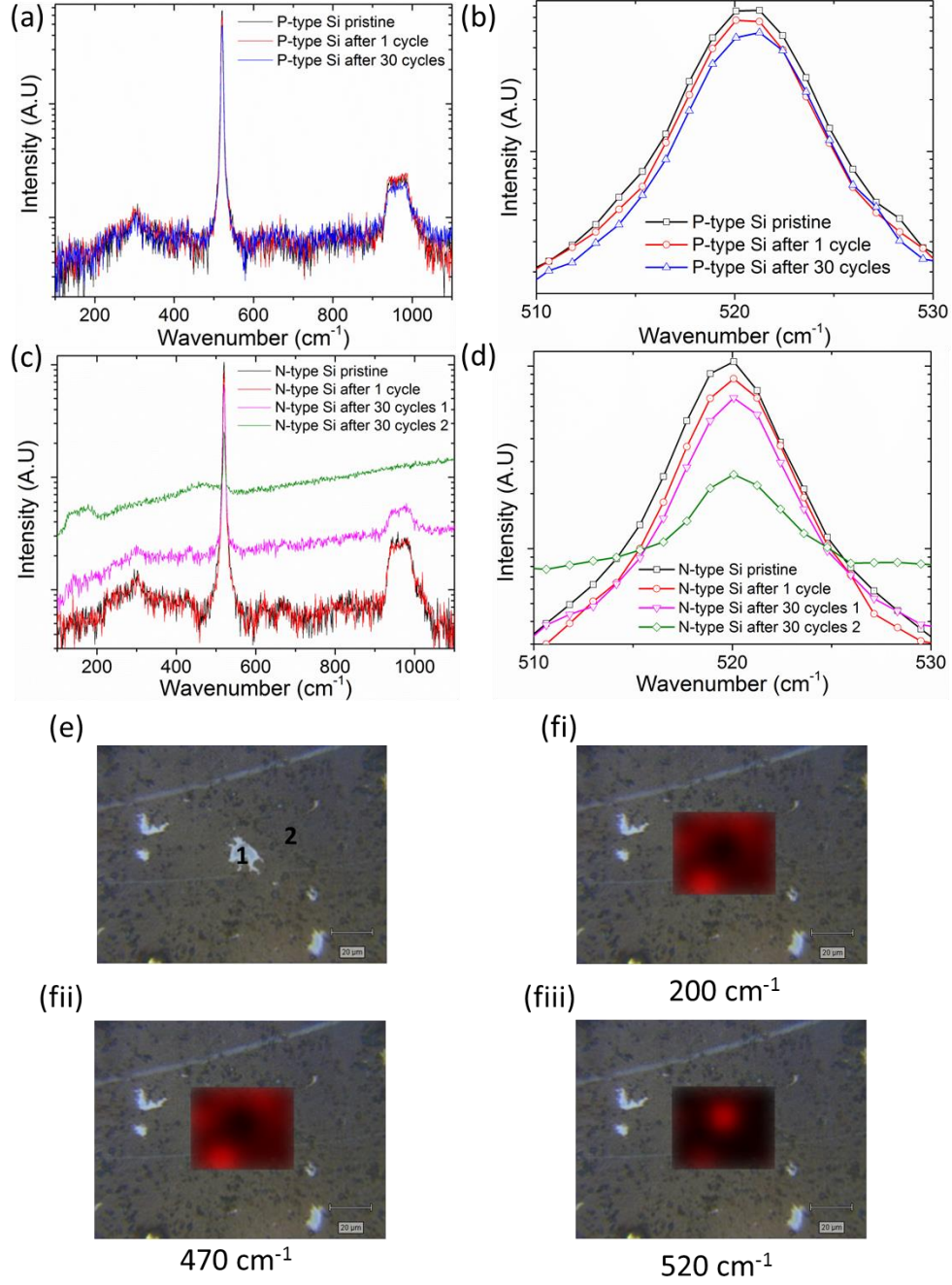


Figure 7. Raman scattering spectra of (a) pristine and (b) cycled p-type Si(100), the reduction in height with cycling of the 520 cm^{-1} peak corresponds to the amorphization of the Si. (c) Raman scattering spectra of pristine and (d) cycled n-type Si(100) with (d) showing the difference in intensity of the TO phonon (520 cm^{-1}) mode. (e) Optical image of the two regions mapped in the n-type Si after 30 cycles. (fi-fiii) Raman mapping of regions within the optical image from (e) at the wavenumbers indicated. The intensity is colour-scaled with red indicating high intensity and black is low intensity).

The spectra confirm that Li insertion into p-type Si(100) results in a polycrystalline phase transition but that the amorphous phase does not form up to 30 cycles. For n-type

Si(100) however, the amorphous phase is formed by the second cycle and is characteristically linked to the structural changes found by microscopy.

E. Galvanostatic charging and discharging

The influence of doping type and density on galvanostatic charging and discharging was also assessed. Figure 8 shows the charge and discharge profiles of (a) p-type and (b) n-type Si(100) for the 1st and 2nd cycle. For electrodes with either dopant type, we characteristically find that the first charge has a different profile to subsequent charges, attributed to the formation of the SEI layer in agreement with the characteristics of the first cycle in a cyclic voltammogram of these electrodes.

In Fig. 8, we note characteristic variations between the n-type and p-type Si(100) charge (insertion) profiles. The measured capacity of the p-type Si and n-type Si decreases dramatically upon cycling. This charge contribution is specifically due to SEI formation which does not largely contribute to the cumulative charge ratio between insertion and extraction of Li on subsequent cycles. The n-type Si exhibits a markedly higher capacity when compared to the p-type Si for the 1st charge and this is a characteristic of the electronic effects on the insertion properties of Li into highly doped n-type Si(100) versus low-doped p-type Si(100).

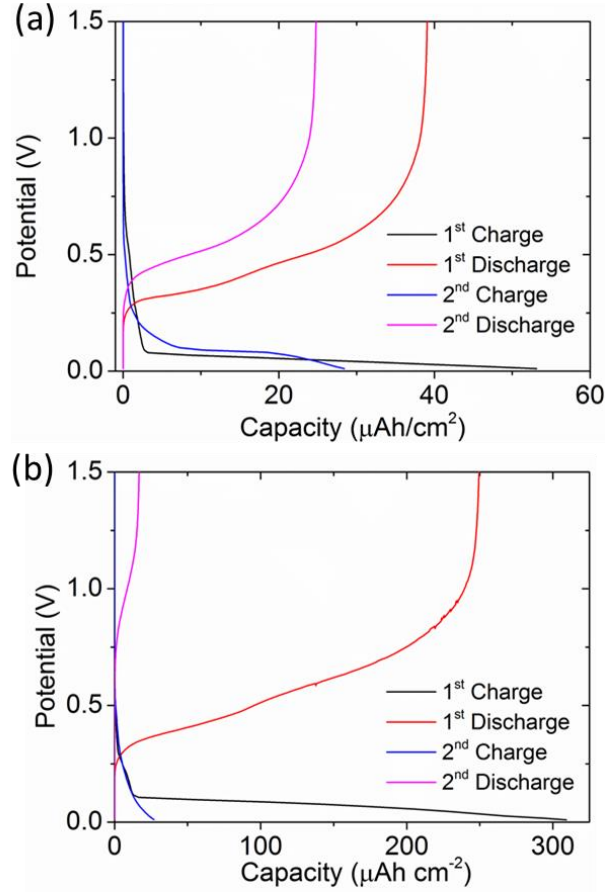


Figure 8. 1st and 2nd charge and discharge profiles of (a) p-type and (b) n-type Si at a constant current density of $20 \mu\text{A cm}^{-2}$.

In Fig. 9(a) and 9(b), we show the influence of doping density on the effective overall capacity of the two anodes with cycling and varying applied current densities of the anodes over these 25 cycles. The applied current was $20 \mu\text{A cm}^{-2}$ for the first five cycles, and this was increased by $5 \mu\text{A cm}^{-2}$ every 5 cycles to maximum of $35 \mu\text{A cm}^{-2}$ for cycles 16-20, for cycles 21-25 the applied current was reduced back to $20 \mu\text{A cm}^{-2}$. In Figs. 9(a) and 9(b), the charge and discharge capacities of the p-type Si and n-type Si are found to decrease dramatically over 25 cycles. Despite having a lower initial charge capacity, the p-type Si is retains a greater percentage of its initial capacity (10.6 %) than the n-type Si (2.8 %) after 25 cycles, this is most likely due to a greater expansion and contraction of the n-type Si during

the first cycle. Without cracking or activation, the p-type Si cannot accommodate higher charge rates, but does retain its capacity at $20 \mu\text{A cm}^{-2}$ after cycling at higher rates. The n-type Si by comparison, can accommodate higher charge rates confirming the influence of a higher doping density for better rate performance.

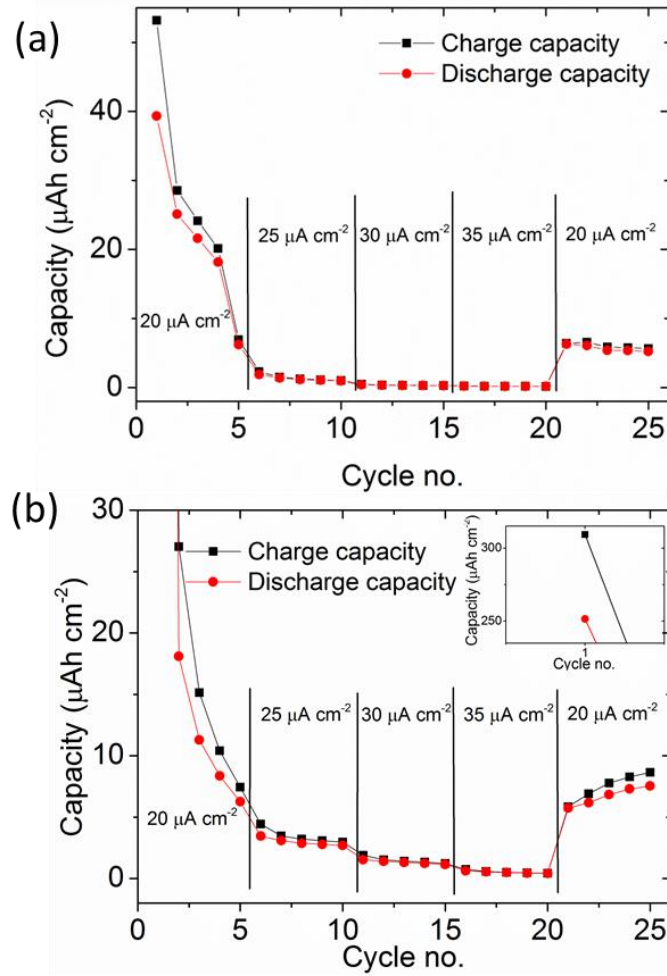


Figure 9. Charge and discharge capacity over 25 cycles at increasing applied current densities of (a) p-type and (b) n-type Si (100) electrodes.

The corresponding Coulombic efficiencies, shown in Fig. 10 increase from a minimum of $\sim 70\%$ to a maximum of $\sim 98\%$ over the 25 cycles. The relatively low efficiency in the first few cycles of both electrodes is attributed to the fraction of charge associated with the formation of the SEI layer. Once the SEI layer is formed, the Coulombic efficiency

generally increases for both electrodes with cycling. The n-type Si(100) characteristically exhibits a lower Coulombic efficiencies at the same rate. Typically discharge process finishing when all the Li-ions are extracted from the very outer surface region layer of Si[91]. The higher Coulombic efficiency of p-type Si(100) compared to its highly doped n-type counterpart signifies an almost complete Li^+ extraction, which is also consistent with the TEM observations where we find negligible variation in the surface region morphology (no cracking) and negligible Li 1s photoelectron signal coming from the flatter p-type lithiated Si surface region. XPS measurements seem to suggest that Li remains within the n-type Si after discharging and this would lead to lower Coulombic efficiencies when compared to the p-type Si. This high efficiency is specifically linked to the doping density and type. The p-type Si(100) band structure and low electronic density limit the rate of redox processes (lower current) at the semiconductor-solution interface; the opposite is observed from n-type highly doped Si(100) surface regions. It can also be seen that the Coulombic efficiency increases with an increasing applied current and decrease again when the applied current is reduced. This increase in Coulombic efficiency with increasing applied current has been reported elsewhere[21, 28, 92-94] where higher rates can promote the Si-alloying process at the expense of the SEI formation for kinetic reasons. SEM images of the surface of p-type and n-type Si(100) electrodes after the variable C-rate constant current experiments (Figs 10(b,c)) show that the p-type Si(100) surface region appears to be roughened but intact, whereas the n-type Si(100) surface region is cracked similar to that shown in Fig. 5 (b). This cracking also correlates to a worse capacity retention of the n-type Si electrode to that of the p-type electrode.

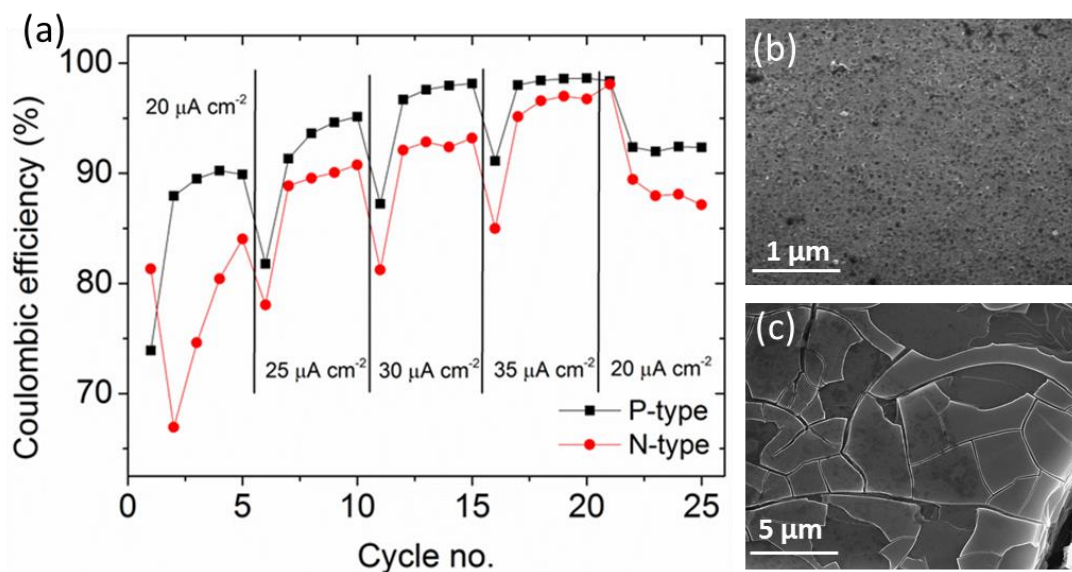


Figure 10. (a) Coulombic efficiencies of the p-type and n-type Si (100) electrodes over 25 cycles, showing the overall increase of the efficiencies with cycling. SEM images of (b) the p-type and (c) the n-type Si after the 25 cycles shown in Fig. 9.

It is interesting to note the drop in Coulombic efficiency for one cycle when the applied current was increased. The voltage-charge relationship from the derivative of the integrated total charge is also related to structural transitions inside electrode materials via the potential-dependent rate of charge transfer[95]. In terms of interpretation and comparison to voltammetric and microscopy analyses of electrode response to Li insertion and extraction, this approach can display sharp peaks for two-phase regions[96] or single broader peaks for single-phase regions, and can reveal the potential at which a certain phase transformation occurs.

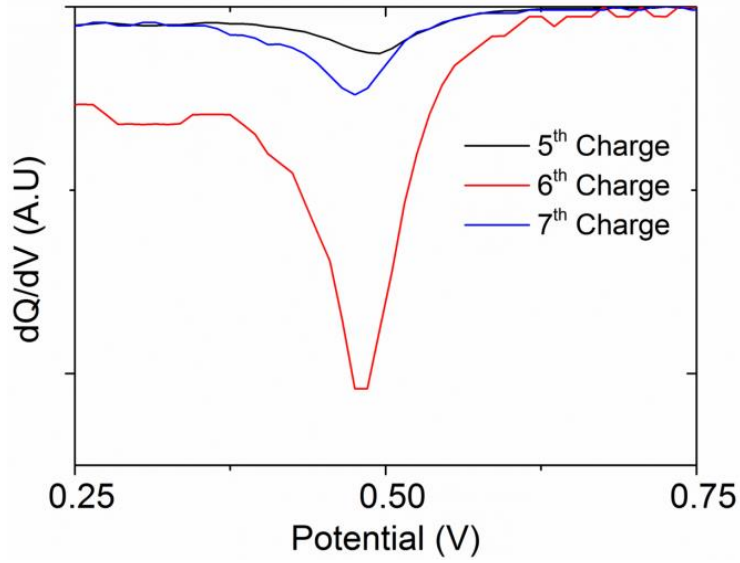


Figure 11. The normalised differential capacity (dQ/dV) curves of the 5th, 6th and 7th charge curves of the p-type Si (100) showing the formation of the SEI layer at approximately 0.5 V.

In Fig. 11, the derivative of the 5th, 6th and 7th charge curves of the p-type Si were plotted to investigate why the Coulombic efficiency would drop between the 5th and 6th cycle but recover almost instantly for the 7th cycle. The derivative of the curves were normalised and plotted. From Fig. 11, we observe that the 6th charge curve has a larger peak at 0.5 V when compared to the peaks of the charge curves of the 5th and 7th cycles. A similar trend was observed whenever the applied current was increased and we can conclude that this is due to the formation of an additional SEI layer, owing to the potential (~ 0.5 V) that we observe the peak, which in turn corresponds to the potential at which the SEI layer typically forms. The formation of an SEI layer is known to reduce Coulombic efficiencies as it typically does not contribute to the discharge of an electrode.

Conclusions

Electrochemical, spectroscopy and high resolution electron microscopy measurements show in detail how the Li insertion and extraction processes at Si(100) surface regions are strongly

influenced by different doping type. Cyclic voltammetry at various potential scan rates confirmed a rate-dependent redox process influenced by the surface region electronic density. Higher currents are found at n-type Si(100) surface regions during Li insertion and extraction which resulted in a cracked lithium silicide phase formation during cycling. At p-type Si(100) surface regions however, a thin, uniform film forms at lower currents, which also shows a consistently high (>70%) Coulometric efficiency for Li extraction.

During Li extraction, p-type Si(100) surface regions do not undergo crack formation in spite of the surface retaining its (poly)crystalline structure during lithiation in the first few cycles before becoming amorphous. Raman scattering and X-ray photoelectron spectroscopy conclusively showed that highly doped n-type Si(100) surface regions retain Li as a silicide and convert to an amorphous phase during early cycles via a polycrystalline phase as a two-step phase conversion process. By monitoring the TO phonon from Si and associated phonon modes associated with amorphous phases, we demonstrated that p-type Si(100) retains some polycrystallinity. The findings shows the succinct dependence of Li insertion and extraction processes for uniformly doped Si(100) single crystals and how the dopant type strongly influences Li insertion and extraction, composition, crystallinity changes and charge capacity.

From a fundamental standpoint, investigations with defined doping densities and types, especially for Si, are useful for examining how semiconducting properties affect the behaviour of Group IV materials as anodes in ion-intercalation based Li-ion batteries. Single crystal Si-based anodes where doping can be spatially defined might allow simultaneous morphology control and mitigate against cracking during long term cycling the causes the materials to become electrochemically inactive. The strongly doping-mediated Li insertion processes into n-type and p-type Si could potentially aid in the design of Si-based anodes where Li insertion can be spatially controlled by rational doping, and maybe important for

nanostructured Si anode materials where different doping densities can help control material conductivity and intercalation rate.

Author information

Corresponding Author

E-mail: c.odwyer@ucc.ie; Tel: +353 (0)21 490 2732; Fax: +353 (0)21 427 4097

Acknowledgments

WMS acknowledges support under the framework of the INSPIRE programme, funded by the Irish Government's Programme for Research in Third Level Institutions, Cycle 4, National Development Plan 2007-2013. CG acknowledges financial support from the Irish Research Council under Award No. RS/2011/797. COD acknowledges support from Science Foundation Ireland under Award no. 07/SK/B1232a from the UCC Strategic Research Fund. The authors acknowledge D. Aureau, M. Bouttemy and A. Etcheberry at Institut Lavoisier de Versailles UMR CNRS 8180, for XPS measurements. This research has received funding from the Seventh Framework Programme FP7/2007-2013 (Project STABLE) under grant agreement n°314508.

References

- [1] M.S. Whittingham, Chemical Reviews 104 (2004) 4271-4302.
- [2] J.M. Tarascon, M. Armand, Nature 414 (2001) 359-367.
- [3] M. Armand, J.M. Tarascon, Nature 451 (2008) 652-657.
- [4] J.R. Dahn, T. Zheng, Y. Liu, J.S. Xue, Science 270 (1995) 590-593.
- [5] M. Winter, J.O. Besenhard, M.E. Spahr, P. Novak, Advanced Materials 10 (1998) 725-763.
- [6] B.A. Korgel, The Journal of Physical Chemistry Letters 5 (2014) 749-750.
- [7] M. Osiak, H. Geaney, E. Armstrong, C. O'Dwyer, Journal of Materials Chemistry A (2014) DOI: 10.1039/C4TA00534A.
- [8] D. Linden, T.B. Reddy, Handbook of Batteries (3rd Edition), McGraw-Hill, 2002.
- [9] C. Liu, F. Li, L.P. Ma, H.M. Cheng, Advanced Materials 22 (2010) E28-E62.
- [10] B. Scrosati, J. Garche, Journal of Power Sources 195 (2010) 2419-2430.

- [11] Y. Yang, S. Jeong, L. Hu, H. Wu, S.W. Lee, Y. Cui, *Proceedings of the National Academy of Sciences* 108 (2011) 13013-13018.
- [12] D.R. Rolison, R.W. Long, J.C. Lytle, A.E. Fischer, C.P. Rhodes, T.M. McEvoy, M.E. Bourga, A.M. Lubers, *Chemical Society Reviews* 38 (2009) 226-252.
- [13] L.Y. Beaulieu, K.W. Eberman, R.L. Turner, L.J. Krause, J.R. Dahn, *Electrochemical and Solid State Letters* 4 (2001) A137-A140.
- [14] C.J. Wen, R.A. Huggins, *Journal of Solid State Chemistry* 37 (1981) 271-278.
- [15] B.A. Boukamp, G.C. Lesh, R.A. Huggins, *Journal of the Electrochemical Society* 128 (1981) 725-729.
- [16] T. Shodai, S. Okada, S.-i. Tobishima, J.-i. Yamaki, *Solid State Ionics* 86-88, Part 2 (1996) 785-789.
- [17] P. Poizot, S. Laruelle, S. Grugeon, L. Dupont, J. Tarascon, *Nature* 407 (2000) 496-499.
- [18] J. Li, J.R. Dahn, *Journal of the Electrochemical Society* 154 (2007) A156-A161.
- [19] L.Y. Beaulieu, T.D. Hatchard, A. Bonakdarpour, M.D. Fleischauer, J.R. Dahn, *Journal of the Electrochemical Society* 150 (2003) A1457-A1464.
- [20] X.-W. Zhang, P.K. Patil, C. Wang, A.J. Appleby, F.E. Little, D.L. Cocke, *Journal of power sources* 125 (2004) 206-213.
- [21] C.K. Chan, H. Peng, G. Liu, K. McIlwrath, X.F. Zhang, R.A. Huggins, Y. Cui, *Nature Nanotechnology* 3 (2008) 31-35.
- [22] J.P. Maranchi, A.F. Hepp, A.G. Evans, N.T. Nuhfer, P.N. Kumta, *Journal of the Electrochemical Society* 153 (2006) A1246-A1253.
- [23] J.P. Maranchi, A.F. Hepp, P.N. Kumta, *Electrochemical and Solid State Letters* 6 (2003) A198-A201.
- [24] M.S. Park, Y.J. Lee, S. Rajendran, M.S. Song, H.S. Kim, J.Y. Lee, *Electrochimica Acta* 50 (2005) 5561-5567.
- [25] J.R. Szczech, S. Jin, *Energy & Environmental Science* 4 (2011) 56-72.
- [26] J. Besenhard, J. Yang, M. Winter, *Journal of Power Sources* 68 (1997) 87-90.
- [27] M. Green, E. Fielder, B. Scrosati, M. Wachtler, J.S. Moreno, *Electrochemical and Solid State Letters* 6 (2003) A75-A79.
- [28] M.N. Obrovac, L.J. Krause, *Journal of the Electrochemical Society* 154 (2007) A103-A108.
- [29] J.H. Ryu, J.W. Kim, Y.E. Sung, S.M. Oh, *Electrochemical and Solid State Letters* 7 (2004) A306-A309.
- [30] M. Gauthier, D. Reyter, D. Mazouzi, P. Moreau, D. Guyomard, B. Lestriez, L. Roué, *Journal of Power Sources*, 256 (2014) 32.
- [31] H.J. Jung, M. Park, Y.G. Yoon, G.B. Kim, S.K. Joo, *Journal of Power Sources* 115 (2003) 346-351.
- [32] S. Ohara, J. Suzuki, K. Sekine, T. Takamura, *Journal of Power Sources* 136 (2004) 303-306.
- [33] W. Xu, J.C. Flake, *Journal of the Electrochemical Society* 157 (2010) A41-A45.
- [34] K. Kang, H.-S. Lee, D.-W. Han, G.-S. Kim, D. Lee, G. Lee, Y.-M. Kang, M.-H. Jo, *Applied Physics Letters* 96 (2010).
- [35] C.K. Chan, R.N. Patel, M.J. O'Connell, B.A. Korgel, Y. Cui, *Acs Nano* 4 (2010) 1443-1450.
- [36] L.-F. Cui, Y. Yang, C.-M. Hsu, Y. Cui, *Nano Letters* 9 (2009) 3370-3374.
- [37] L.-F. Cui, R. Ruffo, C.K. Chan, H. Peng, Y. Cui, *Nano Letters* 9 (2009) 491-495.
- [38] H. Wu, G. Chan, J.W. Choi, I. Ryu, Y. Yao, M.T. McDowell, S.W. Lee, A. Jackson, Y. Yang, L. Hu, *Nature Nanotechnology* 7 (2012) 310-315.
- [39] A. Magasinski, P. Dixon, B. Hertzberg, A. Kvit, J. Ayala, G. Yushin, *Nat Mater* 9 (2010) 353-358.

- [40] L. Hu, H. Wu, S.S. Hong, L. Cui, J.R. McDonough, S. Bohy, Y. Cui, *Chemical Communications* 47 (2011) 367-369.
- [41] M. Gu, Z. Wang, J.G. Connell, D.E. Perea, L.J. Lauhon, F. Gao, C. Wang, *ACS nano* (2013).
- [42] H. Wu, Y. Cui, *Nano Today* (2012).
- [43] C.K. Chan, X.F. Zhang, Y. Cui, *Nano Letters* 8 (2008) 307-309.
- [44] S.W. Lee, M.T. McDowell, J.W. Choi, Y. Cui, *Nano Letters* 11 (2011) 3034-3039.
- [45] X.H. Liu, H. Zheng, L. Zhong, S. Huan, K. Karki, L.Q. Zhang, Y. Liu, A. Kushima, W.T. Liang, J.W. Wang, J.H. Cho, E. Epstein, S.A. Dayeh, S.T. Picraux, T. Zhu, J. Li, J.P. Sullivan, J. Cumings, C.S. Wang, S.X. Mao, Z.Z. Ye, S.L. Zhang, J.Y. Huang, *Nano Letters* 11 (2011) 3312-3318.
- [46] K. Peng, J. Jie, W. Zhang, S.-T. Lee, *Applied Physics Letters* 93 (2008).
- [47] P. Yang.
- [48] W.L. Xu, S.S.S. Vegunta, J.C. Flake, *Journal of Power Sources* 196 (2011) 8583-8589.
- [49] W.L. Xu, J.C. Flake, *Journal of the Electrochemical Society* 157 (2010) A41-A45.
- [50] J.Y. Huang, L. Zhong, C.M. Wang, J.P. Sullivan, W. Xu, L.Q. Zhang, S.X. Mao, N.S. Hudak, X.H. Liu, A. Subramanian, H.Y. Fan, L.A. Qi, A. Kushima, J. Li, *Science* 330 (2010) 1515-1520.
- [51] R. Huang, J. Zhu, *Materials Chemistry and Physics* 121 (2010) 519-522.
- [52] Q.F. Zhang, W.X. Zhang, W.H. Wan, Y. Cui, E.G. Wang, *Nano Letters* 10 (2010) 3243-3249.
- [53] B. Peng, F.Y. Cheng, Z.L. Tao, J. Chen, *Journal of Chemical Physics* 133 (2010).
- [54] Y.S. Jung, K.T. Lee, S.M. Oh, *Electrochimica acta* 52 (2007) 7061-7067.
- [55] Y.H. Xu, G.P. Yin, Y.L. Ma, P.J. Zuo, X.Q. Cheng, *J. Mater. Chem.* 20 (2010) 3216-3220.
- [56] H. Kim, J. Cho, *Nano Letters* 8 (2008) 3688-3691.
- [57] M. Ge, J. Rong, X. Fang, A. Zhang, Y. Lu, C. Zhou, (2013).
- [58] A.A. Arie, W. Chang, J.K. Lee, *Journal of Electroceramics* 24 (2010) 308-312.
- [59] M.H. Kong, J.H. Noh, D.J. Byun, J.K. Lee, *Journal of Electroceramics* 23 (2009) 376-381.
- [60] S. Rousselot, M. Gauthier, D. Mazouzi, B. Lestriez, D. Guyomard, L. Roué, *Journal of Power Sources* 202 (2012) 262-268.
- [61] W. McSweeney, O. Lotty, N. Mogili, C. Glynn, H. Geaney, D. Tanner, J. Holmes, C. O'Dwyer, *Journal of Applied Physics* 114 (2013) 034309.
- [62] W.J. Weydanz, M. Wohlfahrt-Mehrens, R.A. Huggins, *Journal of Power Sources* 81 (1999) 237-242.
- [63] B.R. Long, M.K.Y. Chan, J.P. Greeley, A.A. Gewirth, *The Journal of Physical Chemistry C* 115 (2011) 18916-18921.
- [64] K. Gelderman, L. Lee, S. Donne, *Journal of chemical education* 84 (2007) 685.
- [65] M.T. McDowell, I. Ryu, S.W. Lee, C. Wang, W.D. Nix, Y. Cui, *Advanced Materials* 24 (2012) 6034-6041.
- [66] K. Zhao, M. Pharr, Q. Wan, W.L. Wang, E. Kaxiras, J.J. Vlassak, Z. Suo, *Journal of The Electrochemical Society* 159 (2012) A238-A243.
- [67] R. Fong, U. Vonsacken, J.R. Dahn, *Journal of the Electrochemical Society* 137 (1990) 2009-2013.
- [68] H. Bryngelsson, J. Eskhult, L. Nyholm, M. Herranen, O. Alm, K. Edstrom, *Chemistry of Materials* 19 (2007) 1170-1180.
- [69] M.Y. Ge, J.P. Rong, X. Fang, C.W. Zhou, *Nano Letters* 12 (2012) 2318-2323.
- [70] H. Lindstrom, S. Sodergren, A. Solbrand, H. Rensmo, J. Hjelm, A. Hagfeldt, S.E. Lindquist, *Journal of Physical Chemistry B* 101 (1997) 7717-7722.

- [71] R. van de Krol, A. Goossens, J. Schoonman, *Journal of Physical Chemistry B* 103 (1999) 7151-7159.
- [72] A.J. Bard, L.R. Faulkner, *Electrochemical methods: fundamentals and applications*, Wiley New York, 1980.
- [73] K. Yoshimura, J. Suzuki, K. Sekine, T. Takamura, *Journal of Power Sources* 146 (2005) 445-447.
- [74] T.L. Kulova, A.M. Skundin, Y.V. Pleskov, E.I. Terukov, O.I. Kon'kov, *Journal of Electroanalytical Chemistry* 600 (2007) 217-225.
- [75] A.G. Dylla, J.A. Lee, K.J. Stevenson, *Langmuir* 28 (2012) 2897-2903.
- [76] J. Li, X. Xiao, F. Yang, M.W. Verbrugge, Y.-T. Cheng, *the Journal of Physical Chemistry C* 116 (2011) 1472-1478.
- [77] Q.F. Zhang, Y. Cui, E.G. Wang, *Journal of Physical Chemistry C* 115 (2011) 9376-9381.
- [78] X.H. Liu, L. Zhong, S. Huang, S.X. Mao, T. Zhu, J.Y. Huang, *Acs Nano* 6 (2012) 1522-1531.
- [79] M. Pharr, K. Zhao, X. Wang, Z. Suo, J.J. Vlassak, *Nano letters* 12 (2012) 5039-5047.
- [80] C.-M. Park, J.-H. Kim, H. Kim, H.-J. Sohn, *Chemical Society Reviews* 39 (2010) 3115-3141.
- [81] G.K. Simon, T. Goswami, *Metallurgical and Materials Transactions A* 42 (2011) 231-238.
- [82] W.-J. Zhang, *Journal of Power Sources* 196 (2011) 13-24.
- [83] J. Graetz, C.C. Ahn, R. Yazami, B. Fultz, *Electrochemical and Solid State Letters* 6 (2003) A194-A197.
- [84] S. Ohara, J. Suzuki, K. Sekine, T. Takamura, *Journal of Power Sources* 119–121 (2003) 591-596.
- [85] P. Limthongkul, Y.-I. Jang, N.J. Dudney, Y.-M. Chiang, *Acta Materialia* 51 (2003) 1103-1113.
- [86] T.D. Hatchard, J.R. Dahn, *Journal of the Electrochemical Society* 151 (2004) A838-A842.
- [87] J. Nanda, M.K. Datta, J.T. Remillard, A. O'Neill, P.N. Kumta, *Electrochemistry Communications* 11 (2009) 235-237.
- [88] J.L. Goldman, B.R. Long, A.A. Gewirth, R.G. Nuzzo, *Advanced Functional Materials* 21 (2011) 2412-2422.
- [89] Z. Iqbal, S. Veprek, *Journal of Physics C: Solid State Physics* 15 (1982) 377.
- [90] M.M. Khayyat, G.K. Banini, D.G. Hasko, M.M. Chaudhri, *Journal of Physics D: Applied Physics* 36 (2003) 1300.
- [91] M. Ge, X. Fang, J. Rong, C. Zhou, *Nanotechnology* 24 (2013) 422001.
- [92] A. Gohier, B. Laik, K.H. Kim, J.L. Maurice, J.P. Pereira-Ramos, C.S. Cojocaru, P.T. Van, *Advanced Materials* 24 (2012) 2592-2597.
- [93] H.T. Nguyen, F. Yao, M.R. Zamfir, C. Biswas, K.P. So, Y.H. Lee, S.M. Kim, S.N. Cha, J.M. Kim, D. Pribat, *Advanced Energy Materials* 1 (2011) 1154-1161.
- [94] T. Takamura, S. Ohara, M. Uehara, J. Suzuki, K. Sekine, *Journal of Power Sources* 129 (2004) 96-100.
- [95] A.H. Thompson, *Journal of The Electrochemical Society* 126 (1979) 608-616.
- [96] J.W. Wang, Y. He, F. Fan, X.H. Liu, S. Xia, Y. Liu, C.T. Harris, H. Li, J.Y. Huang, S.X. Mao, T. Zhu, *Nano Letters* 13 (2013) 709-715.